24th INTERNATIONAL CONGRESS ON SOUND AND VIBRATION
23–27 July 2017, London

ICSV24
23-27JULY 2017
LONDON CALLING

PHASE SPACE DYNAMICS OF THERMOACOUSTIC INTERACTIONS DURING VORTEX-ACOUSTIC LOCK-ON

Gurpreet Singh and Sathesh Mariappan
Indian Institute of Technology, Kanpur, Uttar Pradesh-208016, India, email: sathesh@iitk.ac.in
Balasubramanian Singaravelu
SASTRA University, Thanjavur, Tamil Nadu-613401, India

We investigate the dynamics of thermoacoustic interactions associated during vortex acoustic lock-on in the phase space. Experiments are performed in a premixed, gas fueled bluff body stabilized combustor. The geometry of the burner is designed such that vortex shedding from the bluff body is strong. Air flow rate is varied in a quasi-steady manner, for a given fuel flow rate. It is observed that at low air flow rates, the dominant frequency increases linearly with the air flow rate. The obtained Strouhal number matches with the mode associated with vortex shedding from the bluff body. On the other hand, for higher flow rates the dominant frequency remains almost constant with the air flow rate, indicating the acoustic mode of the combustor. It is also found that at these flow rates, vortex shedding process locks on to the frequency of the acoustic mode. Tools from nonlinear time series analysis are applied to study this transition. The attractor is reconstructed in the phase space and its properties are monitored.
Keywords: combustion instability, vortex-acoustic lock-on, time series analysis

1. Introduction

In combustors with backward facing step or ones with bluff body flame holders, vortices are formed when the shear layer at the lip, between the high and low speed streams becomes unstable [1]. These vortices contain unburnt fuel-air mixture on their one side and hot combustion products on the other. They are shed from the flame holders. In this process, fuel-air mixture and hot combustion products come in contact, resulting in sudden heat release, which is a source of acoustic waves. These waves reach the ends of the combustors and reflect back to perturb the flame, establishing a feedback mechanism. At right conditions, these fluctuations can grow resulting in high amplitude discrete tones inside the system, termed as combustion instability. They result in undesirable structural vibrations, high heat fluxes and subsequent failure.

From previous experimental investigations [2, 3], we know that for infinitesimally small velocity perturbations (u') upstream of the flame holder, vortices are shed at the steady state vortex shedding frequency (f_{s0}). In this shedding process, they release energy, causing pressure (p') and velocity fluctuations. The dominant frequency recorded in this case is f_{s0}. The resulting flow perturbations (u') affects subsequent vortex shedding events and the thermoacoustic feedback loop increases the amplitude of the perturbations. As the fluctuations become large, the dominant frequency in oscillations transitions from steady state vortex shedding frequency (f_{s0}) to the acoustic frequency (f_n) of the duct. After this point, vortices are shed at the acoustic frequency of the system. This phenomenon is known as vortex-acoustic lock-on. We observed that few experimental investigations were performed in the past, focusing mainly to understand vortex-acoustic lock-on. A more thorough and systematic experimental investigation is required to understand the fundamental mechanism causing this frequency switch from f_{s0} to f_n.

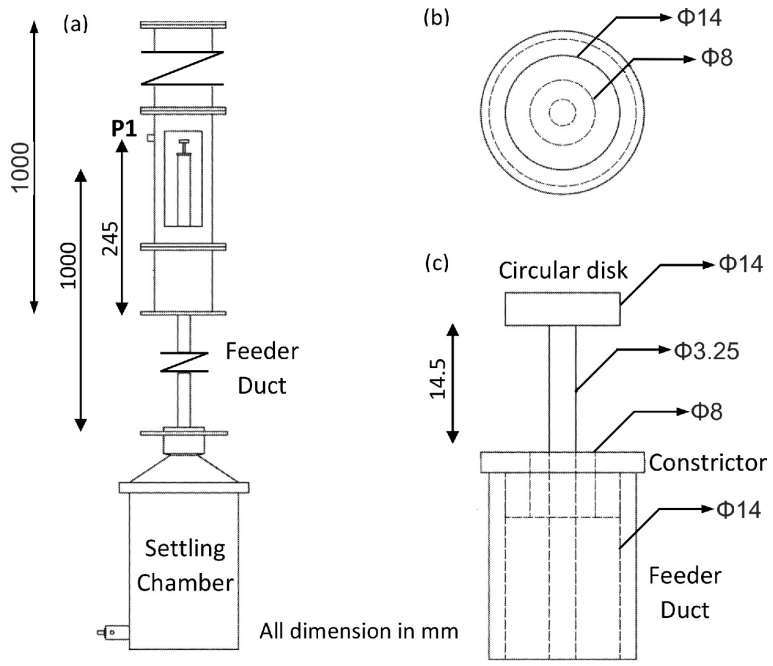

Figure 1: (a) Schematic of the Rijke type combustor used in the present study. (b,c) Zoomed in view of the burner.

Experimental investigations aside, Matveev & Culick (2003)[4] proposed a reduced order model to describe thermoacoustic interactions in a vortex shedding combustor. They modeled the energy release due to vortex breakdown as a kicked oscillator, which is used to simulate the phenomena occurring in real combustors such as mode coupling and lock-on. Again using this model, the stability of the vortex shedding process was studied analytically using Poincaré maps by Singaravelu & Mariappan (2016)[5]. Their prediction on the transition of the dominant frequency was in fair agreement with the experimental results [3]. This gives an hint that using the tools from nonlinear dynamical systems theory is a possible option to understand the mechanism of vortex-acoustic lock-on.

In the recent past, many researchers [6, 7, 8] have successfully used tools from nonlinear time series analysis to understand the transition from combustion noise to periodic oscillations (instability) in lean premixed combustors. This tool has the potential to reveal the existence of rich dynamical behavior and complex attractors in the phase space. The objective of the present investigation is to understand the phase space dynamics of thermoacoustic interactions during the transition in the frequency and vortex-acoustic lock-on.

To meet our objective, we conduct experiments in a laboratory scale vertical Rijke tube type combustor. To improve the circulation strength of the vortices, a bluff body flame holder is used. Pressure fluctuations p' are measured for various air flow rates keeping the fuel flow rate as a constant. First, Fourier transform is used to identify the dominant frequency in the p' oscillations. Later, using nonlinear time series analyses, the measured p' fluctuations are embedded in the phase space after computing the appropriate values of time delay (τ) and embedding dimension (d_e). Then, a topological parameter of the attractor, correlation dimension (d_c) is computed to obtain insights into its nature. The rest of the paper elaborates on the above points in detail.

2. Experimental Setup

The schematics of the experimental setup is shown in Fig. 1. It consists of a premixing settling chamber, where the fuel and air are mixed to obtain a homogeneous mixture. This mixture then passes through a feeder duct (Fig. 1a), having a length and internal diameter of 1 m and 14 mm respectively. A constrictor of internal diameter 8 mm is placed at the end of this duct to accelerate the flow and

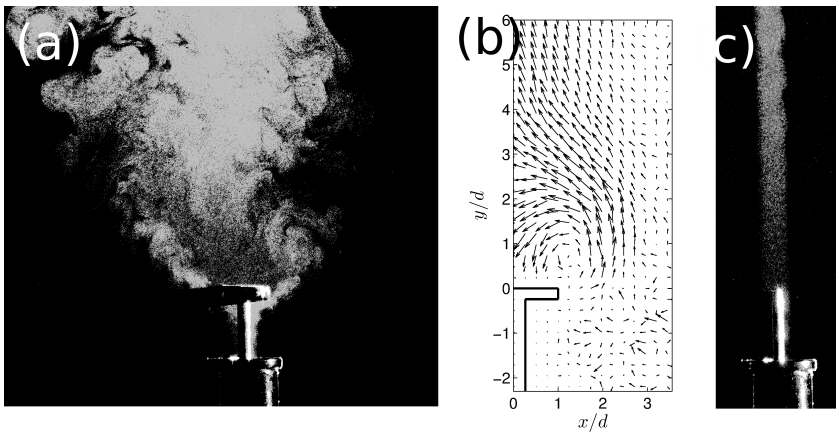

Figure 2: Flow visualization for the case with a) circular disc and without c) circular disc. b) Velocity vectors obtained from PIV in the presence of circular disc. b) Spatial x and y coordinates are nondimensionalized with the radius of the circular disc (d).

initiate vortex shedding. The constrictor is followed by a circular disk of 14 mm diameter and 4 mm thickness, which acts as the bluff body (Fig. 1b,c). It is axially mounted at a distance of 14 mm from the constrictor end. The geometry of the burner is designed such that vortex shedding from the bluff body is strong. The above described feeder duct arrangement is then placed in a Rijke tube, which acts as an acoustic resonator. The dimensions of the Rijke tube are 65 mm $\times$ 65 mm $\times$ 1000 mm.

Liquefied petroleum gas (LPG) having a volumetric composition of 40% propane (C_3H_8) and 60% butane (C_4H_{10}) is used as fuel. Compressed air and fuel are mixed in the settling chamber and passed through the feeder duct. The flow after exiting from the constrictor (placed at the duct exit) impinges on the bluff body (circular disk) providing it a recirculation zone, which stabilizes the flame. The top face of the circular disk is placed at 24.5 cm from the upstream end of the Rijke tube. Experiments are performed at a fuel flow rate, $\dot{v}_f = 1.75$ slpm. Air flow rate is varied from 18 to 50 slpm. Unsteady pressure fluctuations are recorded at a location 24.5 cm (marked as P1 in Fig. $1a$) from the upstream end of the Rijke tube, using a pressure transducer of sensitivity 219.4 mV/Pa and resolution of 0.15 Pa. Recording is performed at a sampling rate 4096 Hz for 5 seconds. A time gap of 30 seconds is given after each incremental change in air flow rate, before recording the data, so as to allow the transients decay.

3. Results and Discussions

In this section, we discuss the dynamics of the system using tools from linear and nonlinear dynamical systems theory. The transition in the frequency and the region of vortex-acoustic lock-on are identified using Fourier transforms. Later, phase space is reconstructed and the associated attractor is characterized from the perspective of nonlinear dynamical systems.

3.1 Vortex-acoustic lock-on

As mentioned already in Section 2, the burner is designed such that strong vortex shedding occurs. In order to identify the exact cause of vortex shedding in the burner, we performed flow visualization study and particle image velocimetry to determine the velocity field in cold flow conditions. Flow visualization is performed for the configuration in the presence (Fig. $2a$) and absence (Fig. $2c$) of the circular disc. We observe vortical patterns to occur and originate near the disc in Fig. $2a$. Furthermore, Fig. $2b$ represents the time averaged velocity vectors around the disc. We again observe the presence of the vortex at the edge of the circular disc. On the other hand, in the absence of the disc, there is no vortex (Fig. $2c$). Hence, the circular disc is the cause of vortex shedding in the present configuration.

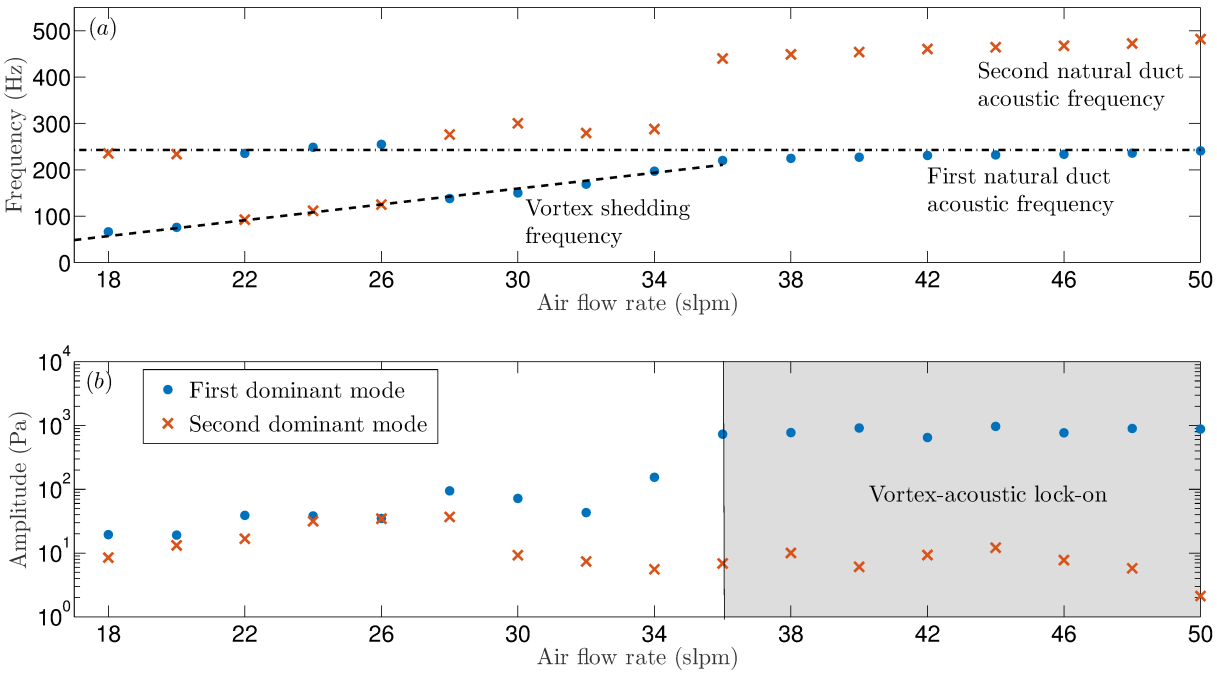

Figure 3: a) Variation of the first (blue dot symbols) and second (red cross symbols) dominant frequency with increase in the air flow rate. Chained horizontal and dashed black lines represent the first duct acoustic and vortex shedding frequencies respectively. b) Variation of the amplitude of the first and second dominant frequency with the air flow rate. Grey region shows vortex-acoustic lock-on.

Moreover, the presence of the constrictor (Fig. 1c) increases the flow velocity at the exit of the feeder duct, producing strong vortex shedding.

The frequencies associated with the first (blue dots) and second (red crosses) dominant mode based on their amplitude of the Fourier spectrum, as we increase the air flow rate are plotted in Fig. 3a. Further, the unsteady pressure time series and the corresponding frequency spectra for four representative cases corresponding to different dynamics are shown in Fig. 4. At very low air flow rate, say $\dot{v}_a = 18$ slpm, the first dominant frequency is 66.25 Hz. The corresponding time signal and the Fourier transform are shown in Fig. 4 (a,b). There is a single dominant peak. As the flow rate is increased, this dominant frequency increases in a linear fashion, indicating that its origin is from vortex shedding process. For the intermediate range of air flow rates ($\dot{v}_a = 24$ slpm), the dominant frequency *suddenly* jumps to a higher value, 248.5 Hz. Later, we show that this corresponds to the first thermoacoustic mode of the system. The corresponding Fourier transform shows two dominant peaks (Fig. 4d). The second dominant peak at this flow rate equals 111.6 Hz, which follow the linear pattern associated with vortex shedding.

On further increasing the flow rate, the vortex shedding mode becomes stronger. At $\dot{v}_a = 30$ slpm, we observe the first dominant frequency equals 150.1 Hz, which also lies on the linear curve for vortex shedding mode. However, as the flow rate is increased to higher value, $\dot{v}_a = 44$ slpm, the first dominant frequency *gradually* increases to 232 Hz. On further increasing the flow rate, this frequency remains almost constant. At $\dot{v}_a = 44$ slpm, the measured steady state temperature at the cold (entrance) and hot (exit) sides are 294 K and 684 K respectively. Since the flame is anchored at the circular disc, which is located at one-fourth of the length of the Rijke tube from the upstream end, the average temperature can be evaluated as $T_{avg} = 294 \times 0.25 + 684 \times 0.75 = 586.5$ K. This corresponds to a speed of sound, $c_{avg} = 485$ m/s. The associated first half wave natural duct mode equals $f_{hw} = c_{avg}/2l = 243$ Hz, which is close to the measured value of 232 Hz. Hence, the observed mode is indeed the first thermoacoustic acoustic mode of the system. The horizontal chained line shown in Fig. 3a corresponds to the value of 243 Hz to indicate a representative acoustic frequency.

To summarize, we make two important observations. In the first one, we identify two qualitatively

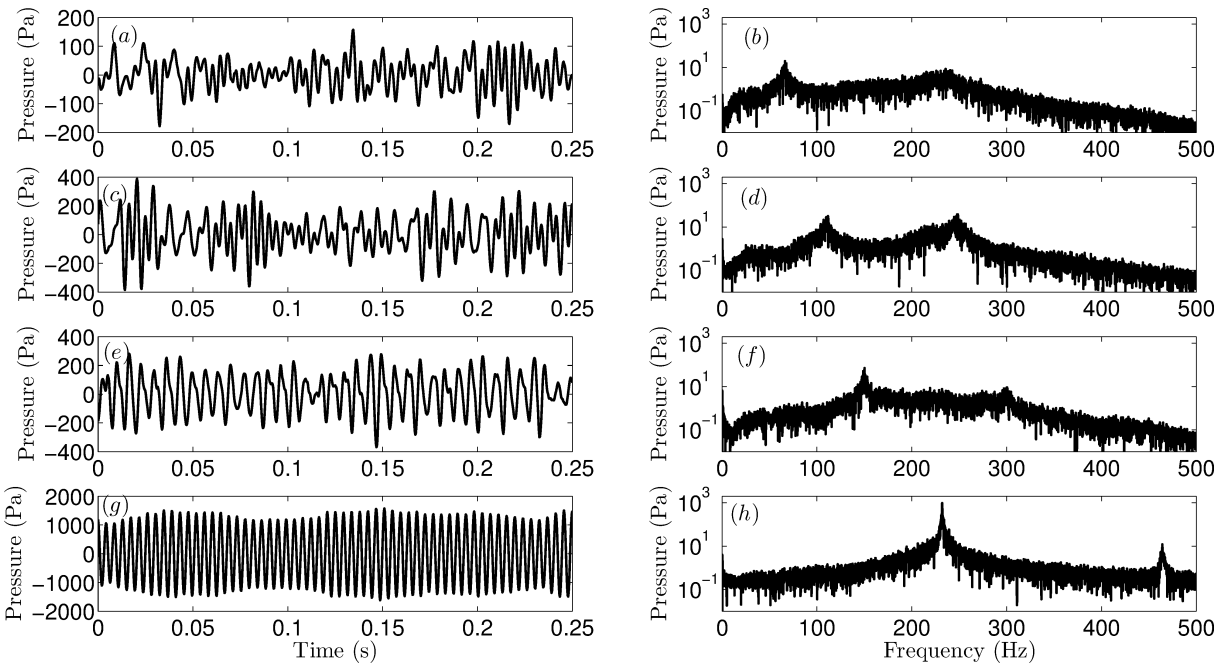

Figure 4: Left: Time series of the pressure signal, right: corresponding Fourier transform. The chosen air flow rates are (a,b) 18 slpm, (c,d) 24 slpm, (e,f) 30 slpm and (g,h) 44 slpm.

different trends in the variation of the dominant frequencies. In trend 1, the frequency increases linearly with the flow rate. Using these data points, a linear fit shown as dashed line in Fig. $3a$ is obtained. From the fit, the Strouhal number St based on the diameter of the circular disc and the flow velocity exiting the constrictor is calculated as 0.17. The Reynolds number based on the diameter of the circular disc for our flow rates lie in the range $6.7 \times 10^3 - 1.74 \times 10^4$. In this range, it was reported by Kiya et. al. 2001 [9], that vortex shedding occurs having a Strouhal number between 0.13 and 0.15. This is in agreement with our fitted value of 0.17. The difference in the numerical value can be due to the fact that the circular disk is placed in the path of a finite width jet and the anchored flame causes baroclinic effects. Nevertheless, the match in the Strouhal number suggests that the observed trend of linear increase in the frequency is indeed due to the vortex shedding behind the circular disk. On the other hand, the second trend of almost constant frequencies with increase in the flow rate is shown to be due to first thermoacoustic mode of the system.

The second observation is the following. There are two locations at which there is a sharp jump in the dominant frequencies. The first occurs at $\dot{v}_a = 22$ slpm, where the first dominant frequency jumps from vortex shedding to the acoustic mode of oscillation. At $\dot{v}_a = 26$ slpm, there is a second jump back to the vortex shedding mode. In this range, $\dot{v}_a =$ 18-26 slpm, the amplitude of the vortex shedding and acoustic modes are equally significant (see Fig. $3b$). We call this as regime I. In the next flow regime $\dot{v}_a =$ 28-34 slpm, the vortex shedding mode becomes more dominant. At $\dot{v}_a =$ 36 slpm, the frequency of the vortex shedding mode approaches the frequency of the acoustic mode. Correspondingly, there is a sharp increase in the amplitude of the oscillations (Fig. $3b$). Further increase in the air flow rate leads to a dominant frequency associated with the acoustic mode of the system. Interestingly, the second dominant mode occurs near a frequency of 450 Hz, which is associated with the second acoustic mode. This result is further strengthened by the observation that the frequency almost remains constant with flow rate and twice the first acoustic mode frequency. In the range $\dot{v}_a =$ 36-50 slpm, the first and the second dominant frequencies are associated only with the acoustic mode, while vortex shedding mode does not appear. This observation suggests that the frequency of vortex shedding from the circular disk changes and locks on to the frequency of acoustic mode. This phenomenon is termed as vortex-acoustic lock-on and this region is named as regime II. In contrast, regime I does not posses vortex-acoustic lock-on and the amplitude of oscillations are

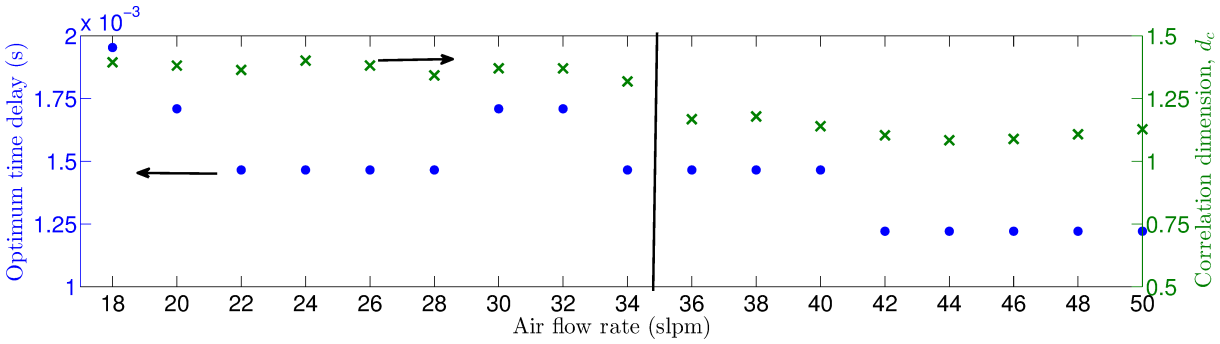

Figure 5: Variation of the optimum time delay τ (blue dot symbols) and correlation dimension (green cross symbols) for various air flow rates.

significantly less in comparison to regime II (Fig. 3*b*).

3.2 Phase space dynamics

In this section, we use tools from nonlinear time series analysis [10] to understand the phase space dynamics of the above discusses behavior. The goal of the analysis is to reconstruct the phase space from the measurements and evaluate the invariant properties of the dynamics. In this study we perform all the analyses using the TISEAN package developed by Hegger et. al. 1999 [11].

3.2.1 Phase space

The measured p' fluctuations are embedded in a phase space with appropriate dimension d_e, termed as embedding dimension. The geometry of the attractor in the phase space is used to understand the dynamics of the system. For a given time series p', the phase space $\mathbf{p_n}$ is reconstructed by, $\mathbf{p_n} = \{p'(t), p'(t+\tau), p'(t+2\tau), \cdots, p'(t+(d_e-1)\tau)$, where τ is the time lag between subsequent series. We compute the average mutual information between the time lagged variables for various time delays. The first minimum in this function is chosen as the optimal time delay τ. The variation of τ with increase in the air flow rate is given in Fig. 5. It is known that τ is related to the frequency content of the signal. For low air flow rate $\dot{v}_a = 18$ slpm, the dominant frequency is the least among other flow rates, which leads to the highest value of the time lag. As the flow rate is increased, dominant frequency due to vortex shedding increases and hence there is a decrease in the value of τ. As discussed before, in the flow rate regime, $\dot{v}_a =$ 22-26 slpm, there are two dominant frequencies: acoustic and vortex shedding modes. The frequency for the acoustic mode is larger than that of vortex shedding mode and stays almost constant with the flow rate. Hence, the associated optimum time lag reaches its lowest value and remains constant with the flow rate.

In the next flow rate regime $\dot{v}_a =$ 28-34 slpm, vortex shedding is the dominant mode of oscillation and still has a lower frequency in comparison to the acoustic mode. Hence, τ begins to increase for $\dot{v}_a =$ 28-30 slpm. From $\dot{v}_a = 32$ slpm, vortex shedding process begins to lock on to the acoustic frequency. Hence, the corresponding value of τ begins to decrease. In the region of vortex-acoustic lock-on ($\dot{v}_a =$ 28-30 slpm), both vortex shedding and acoustic oscillations occur at the first thermoacoustic mode of the system. This leads to a low and constant values of τ. There is also a drop in τ between $\dot{v}_a = 40$ and 42 slpm. This might be due to the appearance of the second thermoacoustic acoustic mode, which has a higher oscillating frequency.

Once the optimum time delay τ is obtained, the phase space is reconstructed by plotting the original and the lagged signal. Figure 6 represents the phase portraits obtained by plotting $p(t) - p(t+\tau)$ (top row) and $p(t) - p(t+2\tau)$ (bottom row). For the case of $\dot{v}_a = 44$ slpm (Fig. 6d,h), only the first thermoacoustic mode is dominant, leading to a portrait containing a limit cycle having one frequency. On the other hand, both the frequencies of vortex shedding and acoustic modes are present

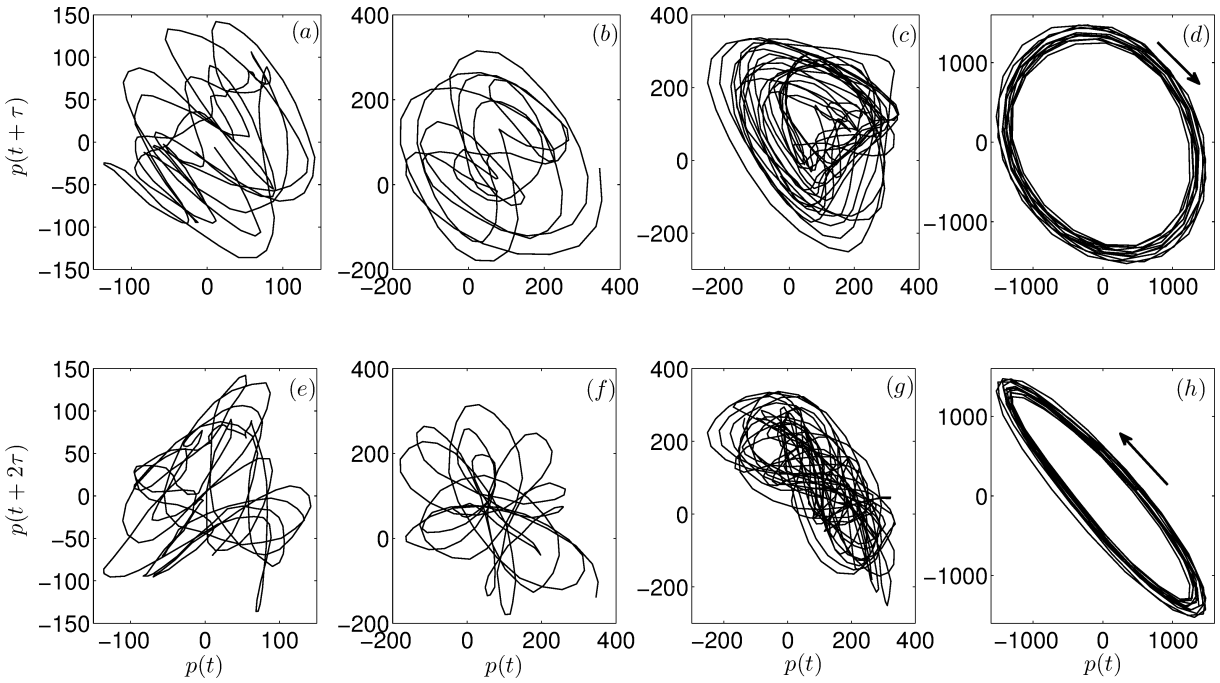

Figure 6: The reconstructed phase space of pressure fluctuations shown for four different air flow rates. (a, e) $\dot{v}_a = 18$ slpm; $\tau = 1.95$ ms, (b, f) $\dot{v}_a = 24$ slpm; $\tau = 1.46$ ms, (c, g) $\dot{v}_a = 30$ slpm; $\tau = 1.71$ ms and (d, h) $\dot{v}_a = 44$ slpm; $\tau = 1.22$ ms. Arrows indicate the direction of time evolution.

for $\dot{v}_a = 30$ & 24 slpm (Fig. 6b-c,f-g). This leads to a portrait having apparent intersections of the trajectory, indicating two frequencies. This behavior is more clear for the case, $\dot{v}_a = 24$ slpm (Fig. 6b,f), as the two modes are equally dominant. In fact, one can observe a distorted Lissajous pattern. For low air flow rate, the amplitude of the oscillations are small, where the background fluctuations becomes relatively significant. This leads to a pattern, where there are many apparent intersections (Fig. 6a,e).

3.2.2 Correlation dimension

The correlation dimension d_c is a quantitative measure of the dimension of the attractor's geometry in phase space. Correlation sum $C(r)$ is defined as the fraction of pairs in the phase space whose distance is smaller than a given threshold r in a given embedding dimension, d_e. In general, $C(r)$ monotonically decreases as $r \to 0$. If $C(r)$ can be approximated by a power law, $C(r) = r^{d_c}$ then d_c is the correlation dimension of the attractor. In this way, for each values of d_e in the range $(1, 30)$, we compute the correlation dimension. The mean result for all the embedding dimensions is taken as the correlation dimension d_c. Figure 5 shows the correlation dimension d_c computed for various flow rates. In all the cases, d_c is close to 1, indicating that the attractor is a limit cycle. During vortex-acoustic lock-on ($\dot{v}_a > 36$ slpm), d_c occurs close to one, indicating a strong limit cycle behavior. There is a jump observed in d_c at the beginning of vortex-acoustic lock-on. Higher values of d_c observed at low flow rates is due to the occurrence of significant background fluctuations.

4. Conclusion

Experiments are performed in a Rijke type combustor to study vortex-acoustic lock-on from the dynamical systems perspective. In this regard, a burner is designed such that strong a vortex shedding from the flame holder occurs. At low air flow rates, we observe the presence of both vortex shedding and acoustic modes of oscillations. For intermediate flow rates, vortex shedding becomes the dominant mode. As flow rate is further increased, the frequency of the vortex shedding mode increases

and merges with the first acoustic mode of the system. At this point, there is a sharp increase in the amplitude of the oscillation is observed. Beyond this flow rate, only the frequency of the acoustic mode is present. The frequency of vortex shedding locks on to the frequency of the acoustic mode. This behavior is identified as vortex-acoustic lock-on. This transition is observed in the phase space by reconstructing the attractor using the tools from nonlinear time series analysis. In particular, we calculated the optimum time delay and the correlation dimension for the attractor. We observed that both these parameters are found to take low constant values in the region of vortex-acoustic lock-on. Further, the presence of the single dominant acoustic frequency during lock-on is depicted by the appearance of an attractor, which does not have apparent intersections. On the other hand, apparent interactions are observed for low flow rates, where both acoustic and vortex shedding frequencies are present.

This work was funded by Science & Engineering Research Board, Department of Science and Technology, India through the project number, SERB/AE/2015317.

References

1. Schadow, K. and Gutmark, E. Combustion instability related to vortex shedding in dump combustors and their passive control, *Progress in Energy and Combustion Science*, **18** (2), 117–132, (1992).

2. Yu, K., Trouvé, A. and Daily, J. W. Low frequency pressure oscillations in a model ramjet combustor, *Journal of Fluid Mechanics*, **232**, 47–72, (1991).

3. Chakravarthy, S. R., Shreenivasan, O. J., Boehm, B., Dreizler, A. and Janicka, J. Experimental characterization of onset of acoustic instability in a nonpremixed half-dump combustor, *The Journal of the Acoustical Society of America*, **122** (1), 120–127, (2007).

4. Matveev, K. I. and Culick, F. E. C. A model for combustion instability involving vortex shedding, *Combustion Science and Technology*, **175** (6), 1059 – 1083, (2003).

5. Singaravelu, B. and Mariappan, S. Stability analysis of thermoacoustic interactions in vortex shedding combustors using poincaré map, *Journal of Fluid Mechanics*, **801**, 597–622, (2016).

6. Gotoda, H., Nikimoto, H., Miyano, T. and Tachibana, S. Dynamic properties of combustion instability in a lean premixed gas-turbine combustor, *Chaos: An Interdisciplinary Journal of Nonlinear Science*, **21** (1), 013124, (2011).

7. Kabiraj, L. and Sujith, R. I. Nonlinear self-excited thermoacoustic oscillations: intermittency and flame blowout, *Journal of Fluid Mechanics*, **713**, 376–397, (2012).

8. Kashinath, K., Waugh, I. C. and Juniper, M. P. Nonlinear self-excited thermoacoustic oscillations of a ducted premixed flame: bifurcations and routes to chaos, *Journal of Fluid Mechanics*, **761**, 399–430, (2014).

9. Kiya, M., Ishikawa, H. and Sakamoto, H. Near-wake instabilities and vortex structures of three-dimensional bluff bodies: a review, *Journal of Wind Engineering and Industrial Aerodynamics*, **89** (14), 1219–1232, (2001).

10. Abarbanel, H. D. I., Brown, R., Sidorowich, J. J. and Tsimring, L. S. The analysis of observed chaotic data in physical systems, *Review of Modern Physics*, **65**, 1331–1392, (1993).

11. Hegger, R., Kantz, H. and Schreiber, T. Practical implementation of nonlinear time series methods: The tisean package, *Chaos: An Interdisciplinary Journal of Nonlinear Science*, **9** (2), 413–435, (1999).